The (ultra) light in the dark: A potential vector boson of 8.7×10^{-13} eV from GW190521

Juan Calderón Bustillo,[1,2,3,*] Nicolas Sanchis-Gual,[4,†] Alejandro Torres-Forné,[5] José A. Font,[6,7] Avi Vajpeyi,[2,3] Rory Smith,[2,3] Carlos Herdeiro,[8] Eugen Radu,[8] and Samson H. W. Leong[1]

[1] *Department of Physics, The Chinese University of Hong Kong, Shatin, N.T., Hong Kong*
[2] *Monash Centre for Astrophysics, School of Physics and Astronomy, Monash University, VIC 3800, Australia*
[3] *OzGrav: The ARC Centre of Excellence for Gravitational-Wave Discovery, Clayton, VIC 3800, Australia*
[4] *Centro de Astrofísica e Gravitação - CENTRA, Departamento de Física, Instituto Superior Técnico - IST, Universidade de Lisboa - UL, Avenida Rovisco Pais 1, 1049-001, Portugal*
[5] *Max Planck Institute for Gravitational Physics (Albert Einstein Institute), Am Mühlenberg 1, Potsdam 14476, Germany*
[6] *Departamento de Astronomía y Astrofísica, Universitat de València, Dr. Moliner 50, 46100, Burjassot (València), Spain*
[7] *Observatori Astronòmic, Universitat de València, C/ Catedrático José Beltrán 2, 46980, Paterna (València), Spain*
[8] *Departamento de Matemática da Universidade de Aveiro and Centre for Research and Development in Mathematics and Applications (CIDMA), Campus de Santiago, 3810-183 Aveiro, Portugal*

Advanced LIGO-Virgo reported a short gravitational-wave signal (GW190521) interpreted as a quasi-circular merger of black holes, one populating the pair-instability supernova gap, forming a remnant black hole of $M_f \sim 142 M_\odot$ at a luminosity distance of $d_L \sim 5.3$ Gpc. With barely visible pre-merger emission, however, GW190521 merits further investigation of the pre-merger dynamics and even of the very nature of the colliding objects. We show that GW190521 is consistent with numerically simulated signals from head-on collisions of two (equal mass and spin) horizonless vector boson stars (aka Proca stars), forming a final black hole with $M_f = 231^{+13}_{-17}\, M_\odot$, located at a distance of $d_L = 571^{+348}_{-181}$ Mpc. The favoured mass for the ultra-light vector boson constituent of the Proca stars is $\mu_{\rm V} = 8.72^{+0.73}_{-0.82} \times 10^{-13}$ eV. This provides the first demonstration of close degeneracy between these two theoretical models, for a real gravitational-wave event. Confirmation of the Proca star interpretation, which we find statistically slightly preferred, would provide the first evidence for a long sought dark matter particle.

I. INTRODUCTION

Gravitational-wave (GW) astronomy has revealed a new population of stellar-mass black holes (BHs) more massive than those known from X-ray observations [1, 2]. This population, with masses of several tens of solar masses, complements the supermassive black holes (SMBHs) lurking in the centre of most galaxies, with masses in the range of $10^5 - 10^{10}\, M_\odot$ [3]. The observation of GW190521 [4] by the Advanced LIGO [5] and Virgo [6] detectors has populated the gap between these two extremes. GW190521 is a short duration signal consistent with a quasi-circular binary black hole (BBH) merger, with mild signs of orbital precession, that left behind the first ever observed intermediate-mass black hole (IMBH), with a mass of $\sim 142 M_\odot$ [4, 7]. This interpretation, provided by the LIGO-Virgo collaborations (LVC), is not without challenges. It implies that at least one of the BHs sourcing GW190521 falls within the pair-instability supernova gap (PISN). Alternative interpretations of GW190521 as an eccentric BH merger lead to the same conclusion [8, 9]. According to stellar evolution, such BHs cannot form from the collapse of a star [10], suggesting that GW190521 is sourced by second generation BHs, formed as a result of previous mergers.

GW190521 is, however, different from previously observed signals. While consistent with a BBH merger, its pre-merger signal, and therefore a putative inspiral phase, is barely observable in the detectors sensitive band, motivating the exploration of alternative scenarios that do not involve an inspiral stage. One such possibility is an extremely eccentric BH encounter, namely a head-on collision (HOC), which we have recently investigated [11]. Within such geometry, however, the high spin of the GW190521 remnant, $a \sim 0.7$, is difficult to reach for HOCs with small mass ratios ($1 < q \equiv m_1/m_2 < 4$) due to the lack of orbital angular momentum and the Kerr limit on the BH spin ($a \leq 1$), imposed by the cosmic censorship conjecture. There exist, however, exotic compact objects (ECOs) not subject to this limit that may mimic BBH signals, leading to a degeneracy in the emitted signals [12].

ECOs have been proposed, e.g., as dark-matter candidates. In this context, some ECOs invoke the existence of hypothetical ultra-light (i.e. sub-eV) bosonic particles. One common candidate is the pseudo-scalar QCD axion, but other ultra-light bosons arise, e.g., in the string axiverse [13]. In particular, vector bosons are

* juan.calderon.bustillo@gmail.com
† nicolas.sanchis@tecnico.ulisboa.pt

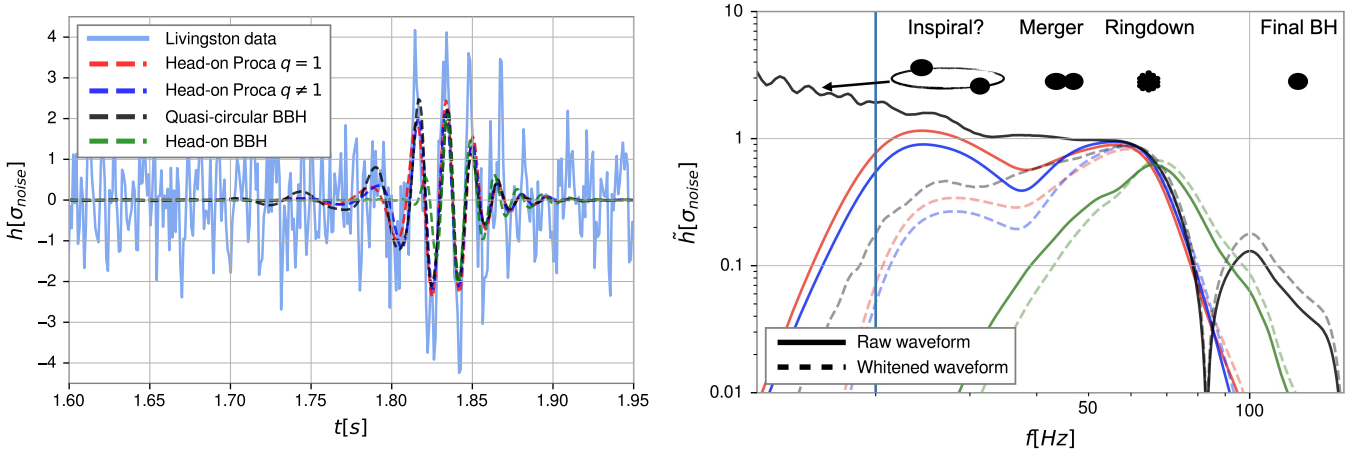

FIG. 1. **Time-series and spectrum of GW190521. Left:** Whitened strain data of the LIGO Livingston detector at the time of GW190521, together with the best fitting waveforms for a head-on merger of two BHs (green), two equal/unequal mass PSs (red and blue) and for a quasi-circular BH merger (black). The time axis is expressed so that the GPS time is equal to $t_{\rm GPS} = t + 1242442965.6069$ s. **Right:** corresponding waveforms shown in the Fourier domain. Solid lines denote raw waveforms (scaled by a suitable, common factor) while dashed lines show the whitened versions. The vertical line denotes the 20 Hz limit, below which the detector noise increases dramatically. Due to this, a putative inspiral signal from a quasi-circular BBH merger (solid black) would be almost invisible to the detector (see dashed grey) and barely distinguishable from PHOC signals (dashed red and blue).

also motivated in extensions of the Standard Model of elementary particles. Such bosons can clump together forming macroscopic entities dubbed bosonic stars. These are amongst the simplest and dynamically more robust ECOs proposed so far and their dynamics has been extensively studied, see *e.g.* [14–17]. Scalar boson stars and their vector analogues, Proca stars [18, 19] (PSs), are self-gravitating stationary solutions of the Einstein-(complex, massive) Klein-Gordon [20] and of the Einstein-(complex) Proca [18] systems, respectively. These consist on complex bosonic fields oscillating at a well-defined frequency ω, which determines the mass and compactness of the star. Unlike other ECOs, bosonic stars can dynamically form without any fine-tuned condition through the gravitational cooling mechanism [21, 22]. While spinning solutions have been obtained for both scalar and vector bosons, the former are unstable against non-axisymmetric perturbations [23]. Hence, we will focus on the vector case in this work. For non-self-interacting bosonic fields, the maximum possible mass of the corresponding stars is determined by the boson particle mass μ_V. In particular, ultra-light bosons within $10^{-13} \leq \mu_V \leq 10^{-10}$ eV, can form stars with maximal masses ranging between $\sim$ 1000 and 1 solar masses, respectively.

We perform Bayesian parameter estimation and model selection on 4 seconds of publicly available data [24] from the two Advanced LIGO and Virgo detectors around the time of GW190521 sampled at 1024 Hz, using at lower frequency cutoff $f_{min} = 11$ Hz (for full details, see the Parameter Estimation section within the Methods). We compare GW190521 to numerical simulations of HOCs, to simulations of equal-mass and equal-spin head-on PS mergers (PHOCs), and to the surrogate model for generically spinning BBH mergers `NRSur7dq4` [25]. Our numerical simulations include the gravitational-wave modes $(\ell, m) = (2, 0), (2, \pm 2), (3, \pm 2)$ while the BBH model contains all modes with $\ell \leq 4$. All PHOCs considered eventually form a BH, emitting less than 0.1% of their mass. We note that in cases with low compactness the final object may not be a Kerr BH but a perturbed PS with continuous, low-frequency GW emission [16, 17]. However, the cases we consider form a Kerr BH with a feeble Proca remnant that does not impact on the GW emission [26].

In addition, to check the robustness of our results, we perform an exploratory study comparing GW190521 to a very limited family of simulations for unequal-mass ($q \neq 1$) head-on PS mergers.

II. RESULTS

Figure 1 shows the whitened strain time series from the LIGO Livingston detector, i.e., after dividing by the detector amplitude spectral density. Overlaid, we show the best fitting (maximum likelihood) waveforms returned by our analysis for PHOCs (in red and blue), HOCs (green) and BBH mergers (black). While the BBH and PHOC waveforms show a similar morphology with slight pre-peak power, the HOC signal is noticeably shorter and has a slightly larger ringdown frequency. These features are more evident in the right panel, where

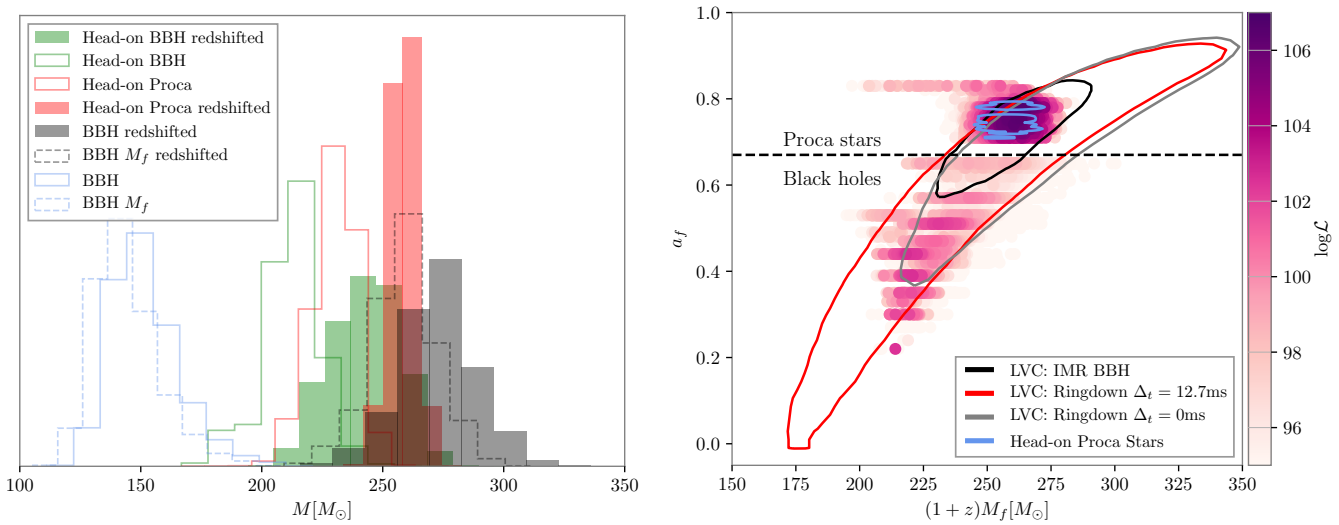

FIG. 2. **Total mass, final mass and final spin of GW190521 according to different source models**. **Left:** Posterior distributions for the total and final mass of GW190521. Filled (empty) histograms denote redshifted (source-frame) values. Dashed histograms denote final masses according to the BBH model. For head-on mergers, we use the total mass as a proxy for the final mass. **Right:** redshifted final mass and spin of GW190521 according to different waveform models, and directly inferred from a ringdown analysis. The contours delimit 90% credible intervals. For head-on PS and BH mergers (PHOCs and HOCs), we plot the samples colored according to their LogLikelihood. The horizontal dashed line denotes an experimental limit for the final-spin of head-on BH mergers that separates then from head-on PS mergers.

we show the Fourier transforms of the same waveforms (dashed) together their raw, non-whitened versions (solid lines). The HOC waveform displays a rapid power decrease at frequencies below its peak due to the absence of an inspiral. In contrast, PHOCs (red and blue) show a low-frequency tail due to the pre-collapse emission that mimics the typical inspiral signal present in the BBH case down to $f \simeq 20$ Hz. Below this limit, the putative inspiral signal from a BBH (solid black) disappears behind the detector noise (dashed grey) making the signal barely distinguishable from that of a PHOC (dashed, red and blue).

The left panel of Fig. 2 shows total mass estimates for GW190521 according to the three mentioned waveform models. The empty histograms show source-frame values while the filled ones show redshifted ones given by $M^z = (1+z)M$, with z the redshift. The dashed histograms denote the final masses obtained by the LVC using the BBH model. For PHOC and HOC, we approximate the final mass by $M_f \simeq M$ due to the negligible mass loss to GWs. For the PHOC case, the redshifted total mass is in good agreement with the BBH final mass while HOCs return slighly lower estimates. The right panel shows the 90% credible intervals for the redshifted final mass and the final spin obtained by the LVC using BBH models covering inspiral, merger and ringdown (IMR, in black) and solely from the ringdown emission; starting at the signal peak (grey) and 12.7 milliseconds later (pink). Overlaid, we show the red-shifted final mass M_f^z and spin a_f obtained by PHOC and HOC models, with the color code denoting the log-likelihood of the corresponding samples.

Due to the absence of an inspiral, HOCs and PHOCs are much less luminous than BBHs, needing a lower initial mass to produce a final BH with the same final as that from a BBH merger. In fact, assuming a BBH scenario yields $M^z_{\rm BBH} = 272^{+26}_{-27}\,M_\odot$ [24] [4] , while we obtain lower values of $M^z_{\rm HOC} = 238^{+24}_{-21}\,M_\odot$ and $M^z_{\rm PHOC} = 258^{+6}_{-8}\,M_\odot$. Taking the latter two as a proxy for the respective final masses, both final mass and spin values estimates lie within the regions estimated by the LVC ringdown analysis $M^z_{\rm BBH,\ Ringdown} = 252^{+63}_{-64}\,M_\odot$ [4], which makes no assumption on the origin of the final BH.

There is, however, a clear separation between HOCs and BBHs/PHOCs in terms of the final spin. Cosmic censorship imposes a bound $a \leq 1$ on the dimensionless spin parameter of a Kerr BH [27]. This, together with the negligible orbital angular momentum in our HOCs, makes it very difficult to produce a BH with the large spin predicted by BBH models. By contrast, PSs are not constrained by $a \leq 1$ and, therefore, can form remnant BHs with higher spins from head-on collisions. Consequently, the final spin and redshifted mass predicted by our best fitting PSs coincide with those predicted by BBH models. In addition, the discussed lack of pre-peak power in HOCs leads to a poor signal match reflected in low values of the log-likelihood, i.e., poor fits, that penalises the model. The top rows of Table I report the Bayesian evidence for our source models. We obtain a relative nat-

Waveform model	$\log \mathcal{B}$	$\log \mathcal{L}_{Max}$
Quasi-circular Binary Black Hole	80.1	105.2
Head-on Equal-mass Proca Stars	80.9	106.7
Head-on Unequal-mass Proca Stars	82.0	106.5
Head-on Binary Black Hole	75.9	103.2

TABLE I. **Bayesian evidence for our GW190521 source models.** We report the natural Log Bayes Factor obtained for our different waveform models and corresponding maximum values of the Log Likelihood. We note that parameter estimation codes *are not* designed to find the true maximum of the likelihood, so that the values we report should be considered as approximate.

ural log Bayes factor $\log \mathcal{B}^{\rm HOC}_{\rm BBH} \sim -4.2$ that allows us to confidently discard the HOC scenario.

Unlike BHs, neutron star and PS mergers do not directly form a ringing BH. Instead, a remnant transient object produces GWs before collapsing into a BH, leaving an imprint in the gravitational signal that is not present for HOCs, before emitting the characteristic ringdown signal. For this reason, PHOCs do not only lead to a final mass and spin fully consistent with the LVC BBH analysis but also provide a better fit to the data than HOCs, reflected by a larger maximum likelihood in Table I.

While BBHs lose around 7% of their mass to GWs, head-on mergers radiate only $\sim 0.1\%$ of it, leading to much lower distance estimates, and consequently, to much larger source-frame masses. Consequently, whereas the LVC model reports a distance of $d_L \sim 5.3^{+2.4}_{-2.6}$ Gpc [4], the PHOCs scenario yields $d_L = 571^{+348}_{-181}$ Mpc, a distance similar to that of GW150914 [1]. This leads to a source-frame final-mass estimate of $\sim 231^{+13}_{-17}\,M_\odot$, 62% larger than the $142^{+28}_{-16}\,M_\odot$ reported by the LVC. The lower distance estimate handicaps the PHOC model with respect to the BBH one if an uniform distribution of sources in the Universe is assumed. Nonetheless, Table I reports a $\log \mathcal{B}^{\rm PHOC}_{\rm BBH} \sim 0.8$, slightly favouring the PHOC model. Relaxing this assumption, leads to an increased $\log \mathcal{B}^{\rm PHOC}_{\rm BBH} \sim 3.4$ (see Supplementary Table IV for a full description of results using this alternative prior). The evidence favouring the PHOC model is accompanied by a sensibly larger value of the log-likelihood, i.e., a better fit to the data. In addition, generically spinning BBHs span a significantly larger parameter space than our PHOC waveforms, which can penalise the former model via the Occam penalty. While we explored several simplifications of the BBH model, as removing spin precession and removing large mass-ratios from the explored parameter space, none of these leads to a statistical preference for the BBH model (for a detailed description, please see Methods). We therefore conclude that, however exotic, the PHOC scenario is slightly preferred despite being intrinsically disfavoured by our standard source-distribution prior.

The inset in the top left of Fig. 3 shows our 2-dimensional 90% credible region for the distance d_L and inclination angle ι of GW190521, assuming a PHOC scenario. The latter is defined as the angle formed by the final spin and the line-of-sight. Contrary to quasi-circular mergers, the GW emission from head-on mergers is not dominated by the quadrupole $(2,2)$ mode [28], but have a similarly strong $(2,0)$ mode [29, 30]. This provides a richer morphology to the signals [31–33] that breaks degeneracies between parameters, e.g., that between the distance and the inclination angle [31, 34, 35] and that between the polarisation angle and the azimuth [32]. The inclusion of this mode in our templates helps to better constrain not only the distance and orientation of the binary but also allows to estimate, for the first time, the azimuthal angle φ describing the location of the observer around the source.

We find that the inclusion of the $(2,0)$ mode disfavours face-on(off) orientations given by $\iota = 0(\pi)$, for which this mode is suppressed, hence suggesting its presence in the signal. By repeating our analysis excluding the $(2,0)$ mode from our templates, we obtain a $\log \mathcal{B} \sim 0.6$, mildly favouring the presence of the $(2,0)$ mode. The inclination of the source, together with the asymmetry in the GW emission produced by this mode, allows to measure the azimuthal angle of the observer, understood as that formed by the collision axis and the projection of the line-of sight onto the plane normal to the final spin. We constrain this to $0.06 < \varphi < 1.40$ radians (see main left panel of Fig. 3), measured in the direction of any of the two PSs spins. To facilitate an interpretation of this measurement, the right panel Fig. 3 shows the 90% credible intervals for the projection of the location of the observer around the source (d_L, ι, φ) (or conversely, distance and source orientation) onto the collision plane. We restrict φ to the first and third quadrants of this plane. This can be physically interpreted as the trajectory of closest PS to Earth being curved towards us due to the frame-dragging induced by the spins, while the furthest one curves away. To the best of our knowledge, this is the first time such measurement is performed.

Assuming a PHOC scenario, we can investigate the physical properties of the hypothetical bosonic field encoded in GW190521, namely its oscillation frequency (normalized to the boson mass) and the boson mass μ_V itself. The corresponding posterior distributions are shown in Fig. 4. We constrain the former to be $\omega/\mu_V = 0.893^{+0.015}_{-0.015}$.

To obtain the boson mass μ_V, on the other hand, one must recall that each PS model is characterized by a dimensionless mass $\mathcal{M}_{\rm PS} = M_{\rm PS}\,\mu_V/M^2_{\rm Pl}$, where $M_{\rm Pl}$ is the Planck mass. Thus, each PS model can only be assigned a physical mass $M_{\rm PS}$ after specifying a physical value for μ_V. Conversely, identifying $M_{\rm PS}$ with (half of)

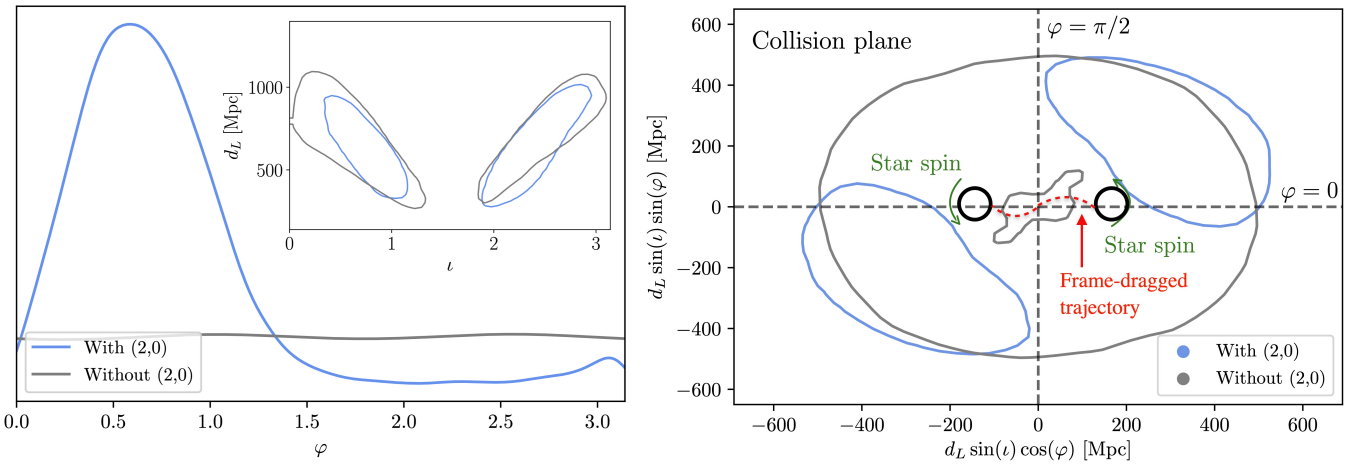

FIG. 3. **Distance and orientation of GW190521 under the assumption of an equal-mass, equal-spin PS merger. Left:** The main panel shows the posterior distribution for the azimuthal angle φ, with $\varphi = 0, \pi$ denoting the line joining the two PSs at the start of the simulation and increasing in the direction of the spin of the individual PSs and final BH. The inset shows the two dimensional 90% credible regions for the inclination angle ι and the luminosity distance d_L. The angle $\iota = 0$ denotes the direction of the final spin. We show results obtained with templates including and omitting the $(2, 0)$ mode. **Right:** 2-dimensional 90% credible regions for the projection of the location (d_L, ι, φ) of the observer around GW190521 onto the collision plane. The azimuthal angle φ grows in the direction of the spin of the stars, while the inclination angle ι is $0(\pi)$ at the center of the plot and evolves toward $\pi/2$ for increasing magnitude of the x and y axis. When including the $(2, 0)$ mode in the analysis, this is restricted to the first and third quadrants of the collision plane. The azimuth angle φ denotes the direction of the spins of the two PSs, to which their trajectories curve towards increasing values of φ due to frame dragging induced by the spins. The size and separation of the stars has been greatly exaggerated to facilitate the interpretation of the plot.

the mass of the final BH in GW190521, $M_{\rm BH}^{\rm final}/2$ (for the simulations with $q = 1$) one obtains μ_V. This yields

$$\mu_V = \left(\frac{\mathcal{M}_{\rm PS}}{M_{\rm BH}^{\rm final}/2}\right) 1.34 \times 10^{-10}\,{\rm eV}, \qquad (1)$$

where $M_{\rm BH}^{\rm final}$ should be expressed in solar masses. Following this reasoning, we constrain the boson mass to $\mu_V = 8.72^{+0.73}_{-0.82} \times 10^{-13}\,{\rm eV}$. In Table II, we summarize the bosonic field and GW190521 parameters, assuming the Proca hypothesis.

Knowing the boson mass, we can estimate the maximum possible mass for a PS described by such ultra-light boson using

$$\left(\frac{M_{\rm max}}{M_\odot}\right) = 1.125 \left(\frac{1.34 \times 10^{-10}\,{\rm eV}}{\mu_V}\right). \qquad (2)$$

This yields $M_{\rm max} = 173^{+19}_{-14}\,M_\odot$. Binaries with lower total masses than this $M_{\rm max}$ would produce a remnant that would not collapse to a BH; therefore, they would not emit a ringdown signal mimicking that of a BBH. This allows us to discard PSs composed of bosons with the above μ_V as sources any of the previous Advanced LIGO - Virgo BBH observations, as the largest (redshifted) total mass among these, corresponding to GW170729, is only around $120\,M_\odot$ [2, 34].

Let us close by testing the robustness of our results. Firstly, while we have only discussed results making use of a standard distance prior (uniform in co-moving volume), Supplementary Table V shows that these are robust against our choice of distance prior.

Secondly, while our PHOC analysis is limited to equal-masses and spins, we performed a preliminary exploration of unequal mass cases, comparing GW190521 to a second family of PHOCs with unequal masses. In these, we fix the oscillation frequency of the bosonic field to a value of $\omega_1/\mu_V = 0.895$, varying ω_2/μ_V along a uniform grid. Our parameter estimates, reported in Table II, are fully consistent with those obtained for the equal-mass case. In particular, we obtain a final BH mass of $M_f = 228^{+16}_{-13}\,M_\odot$ and a boson mass $\mu_V = 8.59^{+0.58}_{-0.59} \times 10^{-13}$ eV. We obtain, however, a notably larger distance estimate $d_L = 700^{+292}_{-279}$ Mpc and slightly a larger evidence of $\log \mathcal{B}^{PHOC}_{BBH} = 1.9$. This indicates that a more in-depth exploration of the full parameter space may be of interest, albeit not impacting too significantly on our main findings.

III. DISCUSSION

We have compared the short GW signal GW190521 to numerical simulations of BH head-on mergers and horizonless bosonic stars known as PSs. We discard the first scenario due to the lack of any pre-merger emission and

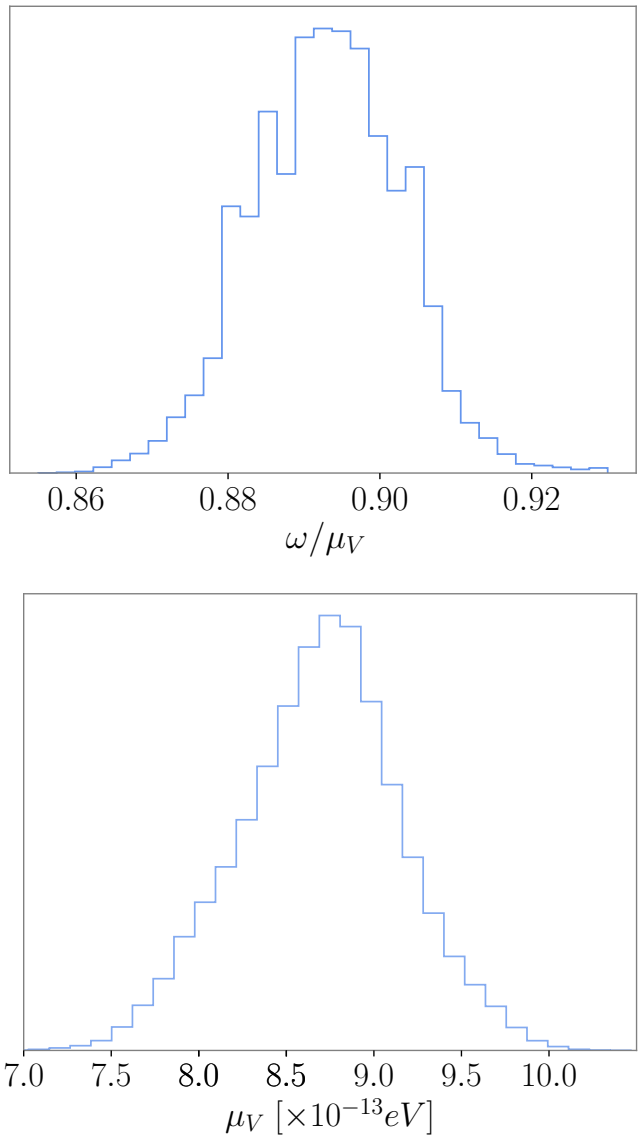

FIG. 4. **Posterior distribution for the values of the bosonic field associated to GW190521.** The top panel shows the oscillation frequency of the bosonic field ω/μ_V. The bottom panel shows the mass of the ultra-light boson μ_V. We assume a merger of two equal-mass and equal-spin Proca stars.

Parameter	$q=1$ model	$q\neq 1$ model
Primary mass	$115^{+7}_{-8}\,M_\odot$	$115^{+7}_{-8}\,M_\odot$
Secondary mass	$115^{+7}_{-8}\,M_\odot$	$111^{+7}_{-15}\,M_\odot$
Total / Final mass	$231^{+13}_{-17}\,M_\odot$	$228^{+17}_{-15}\,M_\odot$
Final spin	$0.75^{+0.08}_{-0.04}\,M_\odot$	$0.75^{+0.08}_{-0.04}$
Inclination $\pi/2-\lvert\iota-\pi/2\rvert$	$0.83^{+0.23}_{-0.47}$ rad	$0.58^{+0.40}_{-0.39}$ rad
Azimuth	$0.65^{+0.86}_{-0.54}$ rad	$0.78^{+1.23}_{-1.20}$ rad
Luminosity distance	571^{+348}_{-181} Mpc	700^{+292}_{-279} Mpc
Redshift	$0.12^{+0.05}_{-0.04}$	$0.14^{+0.06}_{-0.05}$
Total / Final redshifted mass	$258^{+9}_{-9}\,M_\odot$	$261^{+10}_{-11}\,M_\odot$
Bosonic field frequency ω/μ_V	$0.893^{+0.015}_{-0.015}$	$(*)0.905^{+0.012}_{-0.042}$
Boson mass μ_V $[\times 10^{-13}]$	$8.72^{+0.73}_{-0.82}$ eV	$8.59^{+0.58}_{-0.57}$ eV
Maximal boson star mass	$173^{+19}_{-14}\,M_\odot$	$175^{+13}_{-11}\,M_\odot$
Evidence for $(2,0)$ mode	$\log\mathcal{B}\simeq 0.6$	—

TABLE II. **Parameters of GW190521 assuming a head-on merger of Proca stars.** In the the first column we assume equal masses and spins. In the second column we allow for unequal masses, fixing the primary oscillation frequency to $\omega_1/\mu_V=0.895$ and varying the second on an uniform grid. We estimate the secondary oscillation frequency ω_2/μ_V. We report median values and symmetric 90% credible intervals.

to the high spin of the GW190521 remnant BH. We have shown that GW190521 is consistent with an equal-mass head-on merger of PSs, inferring an ultralight boson mass $\mu_V\simeq 8.72\times 10^{-13}$ eV.

We estimate a final redshifted mass and spin consistent with those predicted the LVC assuming a "vanilla" BBH source, which involves a BH component populating the PISN gap. While this may be addressed by assuming that GW190521 is a second-generation merger, there are no predictions of a mass gap in bosonic star formation and distribution in the early Universe that, however exotic, could lead to a similar situation in the case of PSs.

Such ultralight boson particle would spontaneously trigger the superradiant instability in the vicinity of stellar BHs, spinning them down. Current constraints on the boson mass are obtained from the lack of GW emission associated with the superradiance instability and from observations of the spin of astrophysical BHs [36–38]. These constraints, however, apply to *real* bosonic fields. When the bosonic field is complex, as in our case, the bosonic cloud around the BH does not decay by GW emission. In fact, a stationary and axisymmetric Kerr BH with bosonic hair forms [39–41]. These configurations are, themselves, unstable against superradiance [42], but the non-linear development of the instability is too poorly known to establish meaningful constraints on the complex bosons - see, however [43].

Assuming that the boson mass μ_V is unique, our results exclude that PSs below $\sim 170\,M_\odot$ can collapse into remnant ringing BH, due to the low compactness of the stars, excluding all previous GW observations as PS mergers. Our simulations show that the collisions of PS models with $\omega/\mu_V\gtrsim 0.95$ form a perturbed spinning PS that oscillates and emits a continuous low-frequency GW signal.

While our study has mostly focused on head-on mergers of equal-mass stars with equal spins, these suffice to fit GW190521 as closely as state-of-the art BBH models,

being slightly favoured from a Bayesian point of view. While this restriction leads to narrow parameter distributions, the future development of more complex configurations like quasi-circular mergers shall reveal, for instance, a larger range of boson masses consistent with GW190521. To evolve such configurations, however, constraint-satisfying initial data is needed to obtain accurate waveforms, which is currently unavailable. In the head-on scenario, with sufficiently large initial separation D, the constraints violations are largely reduced by construction using the superposition data [30].

The existence of an ultra-light bosonic field would have profound implications in science, from astrophysics and cosmology to theoretical and high-energy physics. It could account for, at least, part of dark matter, as it would give rise to a remarkable energy extraction mechanism from astrophysical spinning BHs, eventually forming new sorts of "hairy" BHs. Not less exciting would be its impact on theoretical particle physics, as a guide towards beyond the standard model physics, possibly a hint towards the stringy axiverse.

While GW190521 does not allow to clearly distinguish between the BBH and PS scenarios, future louder GW observations in the IMBH range shall allow to better resolve the nature of the source, leading to the confirmation or rejection of the existence of the ultra-light vector boson discussed here.

ACKNOWLEDGEMENTS

The authors thank Fabrizio Di Giovanni, Tjonnie G.F. Li and Carl-Johan Haster for useful discussions. The analysed data and the corresponding power spectral densities are publicly available at the online Gravitational Wave Open Science Center [24]. LVC parameter estimation results quoted throughout the paper and the corresponding histograms and contours in Fig. 2 have made use of the publicly available sample release in `https://dcc.ligo.org/P2000158-v4`. JCB is supported by the Australian Research Council Discovery Project DP180103155 and by the Direct Grant from the CUHK Research Committee with Project ID: 4053406. JAF is supported by the Spanish Agencia Estatal de Investigación (PGC2018-095984-B-I00) and by the Generalitat Valenciana (PROMETEO/2019/071). This work is supported by the Center for Research and Development in Mathematics and Applications (CIDMA) through the Portuguese Foundation for Science and Technology (FCT - Fundação para a Ciência e a Tecnologia), references UIDB/04106/2020, UIDP/04106/2020, UID/FIS/00099/2020 (CENTRA), and by national funds (OE), through FCT, I.P., in the scope of the framework contract foreseen in the numbers 4, 5 and 6 of the article 23, of the Decree-Law 57/2016, of August 29, changed by Law 57/2017, of July 19. We also acknowledge support from the projects PTDC/FIS-OUT/28407/2017 and CERN/FIS-PAR/0027/2019. This work has further been supported by the European Unions Horizon 2020 research and innovation (RISE) programme H2020-MSCA-RISE-2017 Grant No. FunFiCO-777740. The authors would like to acknowledge networking support by the COST Action CA16104. The authors acknowledge computational resources provided by the LIGO Laboratory and supported by National Science Foundation Grants PHY-0757058 and PHY0823459; and the support of the NSF CIT cluster for the provision of computational resources for our parameter inference runs. This manuscript has LIGO DCC number P-2000353.

METHODS

A. Numerical Simulations

Bosonic stars, and in particular Proca stars, are fundamentally different from BHs and neutron stars. For the former the angular momentum J can vary continuously for a given mass M. In contrast, in the bosonic case, the value ω/μ_V determines the mass (as function of μ_V) and the compactness of the model, but also the angular momentum. Therefore, a given value of ω/μ_V only allows one (M, J) pair. In addition, the angular momentum is quantized and determined by an integer m, the azimuthal angular momentum number. This property reduces the space of parameters of bosonic stars. While $m = 0$ corresponds to the non-spinning solutions, models with $m \geq 2$ are unstable against non-axisymmetric perturbations [23]. Therefore, we restrict our study to PSs with $m = 1$.

To perform the numerical evolutions we have used the Einstein Toolkit infrastructure [44–46] with the Carpet package [47, 48] for mesh-refinement capabilities. The initial data for the BH head-on collision are calculated using the TwoPunctures thorn [49]. The Proca equations are solved using a modification of the Proca thorn [50] to include a complex field. We have performed numerical simulations of head-on collisions of equal mass PSs. The initial data consists in the superposition of two solutions separated by $D = 40/\mu_V$, in geometric units, to reduce the initial constraint violations. In total we have evolved 77 models with different frequency ω, total mass, angular momentum and compactness. In Fig. 5, we show the time evolution of the energy density for a PS with $\omega/\mu_V = 0.8925$.

Numerical simulations extract the gravitational-wave emission in terms of the Weyl curvature component, ψ_4. Therefore, it is necessary to integrate twice in time to obtain the strain h. This process is not trivial and can produce non-linear drifts in the resulting strain [51]. To avoid these issues, we integrate the ψ_4 component in frequency domain, introducing a small regularization term to avoid the singularity at $f = 0$ Hz. Then we apply a high-pass filter to reduce the energy contained in frequencies lower than a chosen cutoff.

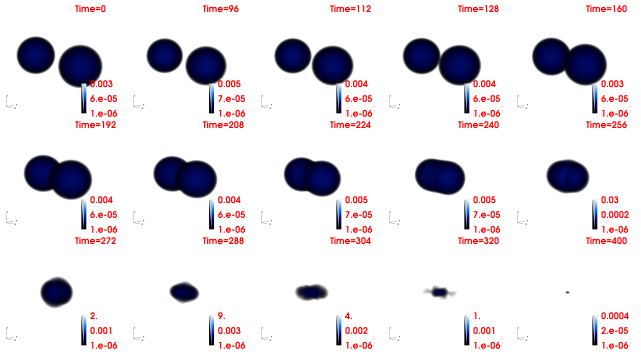

FIG. 5. **Snapshots of the time evolution of the energy density during the head-on collision of two PSs with $\omega/\mu_V = 0.8925$.** Time is given in code units.

B. Parameter Estimation

In this section we provide details regarding our analysis set-up and our parameter estimation procedure. In particular, we explain in detail how continuous parameter distributions are obtained from a set of discrete simulations for PSs and BH head-on mergers, as well as the corresponding evidences and Bayes' Factors. We also discuss the comparison of the evidence for these PS models to that of BBHs.

1. *Data*

We perform parameter estimation on GW190521 using the software `bilby` [52] together with the `cpnest` nested sampling algorithm [53]. We analyse four seconds of publicly available data around the trigger time of GW190521 [24], sampled at 1024 Hz, using the corresponding power spectral density computed by BayesWave [54, 55].

2. *Summary of Bayesian Inference*

The posterior probability for a set of source parameters θ, given a stretch of data d, is given by

$$p(\theta|d,\mathcal{M}) = \frac{\pi(\theta)\mathcal{L}(d|\theta,\mathcal{M})}{\mathcal{Z}(d|\mathcal{M})}, \tag{3}$$

where $\mathcal{L}$ denotes the standard frequency-domain likelihood commonly used for gravitational-wave transients [56, 57]

$$\log\mathcal{L}(d|\theta,\mathcal{M}) = -\frac{1}{2}(d-h_{\mathcal{M}}(\theta)|d-h_{\mathcal{M}}(\theta)). \tag{4}$$

Here, $h(\theta)$ denotes a waveform template for parameters θ, according to the waveform model $\mathcal{M}$. In our case we consider three models, respectively representing quasi-circular binary black hole mergers (BBH), head-on black-hole mergers (HOC) and head-on Proca Star mergers (PHOC). As usual, the operation $(a|b)$ denotes the inner product [58]

$$(a|b) = 4\Re\int_{f_{\rm min}}^{f_{\rm max}} \frac{\tilde{a}(f)\tilde{b}(f)}{S_n(f)}df, \tag{5}$$

where $S_n(f)$ denotes the one sided power spectral density of the detector noise, and $f_{\rm min}$ and $f_{\rm max}$ are respectively the low and high frequency cutoffs of the detector data. The factor $\pi(\theta)$ denotes the prior probability for the parameters θ and the factor $\mathcal{Z}(d|\mathcal{M})$ is known as the evidence for the model $\mathcal{M}$. This is given by the integral of the numerator of Eq.3 across all the parameter space covered by the model

$$\mathcal{Z}(d|\mathcal{M}) := \mathcal{Z}_{\mathcal{M}} = \int \pi(\theta)\mathcal{L}(d|\theta,\mathcal{M})d\theta. \tag{6}$$

Given two models A and B, the degree of preference for model A over model B is given by the Bayes' Factor

$$\mathcal{B}^A_B = \frac{\mathcal{Z}_A}{\mathcal{Z}_B}. \tag{7}$$

Throughout the main text, we refer to $\log(\mathcal{Z}_A)$ and $\log(\mathcal{Z}_B)$ as the "Log Bayes Factor" for each of the models (with respect to the noise, i.e., no-signal hypothesis) and to $\log(\mathcal{Z}_A) - \log(\mathcal{Z}_B)$ as the relative Log Bayes Factor $\log\mathcal{B}^A_B$. It is common to say that the model A is strongly preferred wrt. B when the $\log\mathcal{B}^A_B > 5$. This is, when model A is ~ 150 times more probable than model B.

3. *Prior choices*

Our three models cover different parameter spaces. As usual, the BBH model covers a continuous 15-dimensional parameter space Θ formed by the total mass M, the mass ratio q, the six individual spin components $(\vec{a}_1, \vec{a}_2)$, the two orientation angles (ι, φ), the two sky-localisation angles, the luminosity distance d_L, the polarisation angle and the time of arrival. However, our HOC and PHOC models cover only a discrete set of spins and mass ratios, sharing all the other parameters with the BBH model.

For the case of the HOC and PHOC models we cannot sample over the two individual masses of the binary (as it is common practice) as our simulations only cover a discrete range of mass ratios. Since these simulations scale trivially with the total mass, it is natural to place an uniform prior on it. We choose an uniform prior in $[100, 500]M_\odot$ for all of our models. In addition, we place standard priors on the source orientation, sky-location and polarisation angles. Our PHOC simulations are restricted to mass-ratio $q = 1$ and equal-spins, while for

the BBH case we place an uniform prior in mass-ratio together with the usual isotropic prior for the two individual spins. For the HOC case, our simulations distribute in a non-uniform way in both mass-ratio and spins, as we produced them in a systematic way trying to maximise the likelihood (see more details in the subsection 6. "Evidence for Head-on BBHs").[1] Finally, as we indicate in the main text, we explore two different distance priors. The first one assumes an uniform distribution of sources in co-moving volume. Since this prior will favour large distances, it will prefer loud sources over weak ones, even if both can fit the data equally well. While this is reasonable and also common practice, we try to gauge this away by using also a prior uniform in distance that does not favor loud sources. Finally, we sample the parameter space using the algorithm CPNest [53] and set minimum and maximum frequencies of 11 and 512 Hz for our analysis.

4. Computing evidences and Bayes Factors for Proca Stars

Since the BBH model covers a continuous parameter space, it is trivial to compute the integral in Eq.6 across all the space $\bar{\Theta}$. However, for the case of HOCs and PHOCs we obtain a discrete set of evidences $\mathcal{Z}_{\bar{\Theta}}$ for each set of mass-ratios and spins, which we shall collectively denote as $\bar{\Theta}$. In order to find the evidence corresponding to these models, we need to chose a suitable integration element $d\bar{\Theta}$ to perform the discrete integration over these parameters. While this is intricate for the case of HOC, which we discuss later, for the specific case of PHOCs we can take advantage of the extra parameter ω/μ_V that describes the oscillation frequency of the bosonic field. Since our simulations span an uniform grid in this parameter, we compute the corresponding global evidence as:

$$\mathcal{Z}_{\rm PHOC} \approx \sum \mathcal{Z}_\omega d\omega = \sum \mathcal{L}(d|\omega, {\rm PHOC})\, \pi(\omega)\, d\omega, \quad (8)$$

with

$$\mathcal{L}(d|\omega, {\rm PHOC}) = \int \mathcal{L}(d|\omega, \hat{\theta}, {\rm PHOC})\, \pi(\hat{\theta})\, d\hat{\theta}. \quad (9)$$

Here, $\hat{\theta}$ denotes the extrinsic parameters plus the total mass, so that $\Theta = \bar{\Theta} \cup \hat{\theta}$.

5. The size of the parameter space and the Occam factor

When comparing the BBH and PHOC models, it is important to note that two main factors determine the value of the corresponding evidences. The first one is how well the model can fit the data. Parameters yielding good fits will yield large values of $\log \mathcal{L}$, and vice versa. In particular, note that $\mathcal{Z}$ is bounded by, e.g.,

$$\mathcal{Z}_{\mathcal{M}} \leq \int \pi(\theta) \mathcal{L}_{Max} d\theta. \quad (10)$$

, with $\log \mathcal{L}_{Max}$ denoting the maximum value of the likelihood across the parameter space. Second, the act of integrating implies that the model may explore regions of the parameter space with poor contributions to the integral. Since $\int \pi(\theta) d\theta = 1$ exploring "useless" portions of the parameter space leading to poor fits causes to a reduction of $\mathcal{Z}_{\mathcal{M}}$. This penalty is known as the *Occam factor*.

Because of our limited computational resources, we only performed enough PS simulations to reconstruct the full posterior distribution for the parameter ω/μ, shown in Fig.4. As a consequence, we are not exploring a vast parameter space that may provide poor fits to the data, somewhat minimising the Occam Factor and somehow optimising $\mathcal{Z}_{\rm PHOC}$. Meanwhile, the BBH model covers all the parameter space allowed by the model, leading to an increased Occam Factor and a consequent reduction of $\mathcal{Z}_{\rm BBH}$. Here we explore some simplifications of the BBH model that shall reduce the Occam penalty, potentially increasing the evidence for the model and reduce the relative evidence in favour of our PHOC model. The results are summarised in Table III, and we describe them in the following.

1. **Aligned spins:** The model NRSur7dq4 includes the effect of orbital precession. This effect is described by the 6 spin components of the two BHs, which greatly increases the explored parameter space wrt., that of our PHOC model. We study the effect of restricting the spins to be (anti-)aligned with the orbital angular momentum, therefore removing the impact of precession and eliminating 4 parameters. Doing so, we find $\log \mathcal{B}^{\rm BBH}_{\rm BBH,AS} = 3$ [2], accompanied with a much reduced maximum log-likehood of 98.8. This shows that spin-precession adds a *necessary* complication to the model. Removing this effect increases the evidence for PHOC to $\log \mathcal{B}^{\rm PHOC}_{\rm BBH,AS} = 3.8$.
2. **Mass ratio:** The model NRSur7dq4 covers the mass-ratio range $q \in [1, 4]$. However, the LVC results show that mass ratios $q > 2$ are not well supported by the data [4], therefore adding a parameter range to the model that will certainly increase the Occam factor and penalise the model.

[1] Given the low Bayes' Factors obtained for HOCs, this does not have any impact on the conclusions of our study.

[2] This corresponds to a $\log_{10} \mathcal{B}^{\rm BBH}_{\rm BBH,AS} \simeq 1.3$. The LVC reported 1.06 [4]. Note, however, that while the LVC uses a prior uniform in component masses, we use a prior uniform in total mass and mass ratio.

We perform a second run restricting $q \in [1,2]$. As expected we find a slightly increase evidence, so that $\log \mathcal{B}^{\rm BBH},{}^{q\leq 2}_{q\leq 4} = 0.6$. This slightly reduces the evidence for PHOCs to $\log \mathcal{B}^{\rm PHOC},{}^{q=1}_{q\leq 2} = 0.2$ and $\log \mathcal{B}^{\rm PHOC},{}^{q\neq 1}_{q\leq 2} = 1.3$, but still favours this scenario.

We further restrict the mass ratio to $q = 1$ for the NRSur7dq4 model. The motivation for this is two-fold. First, this is the mass ratio of our primary PHOC model. Second, this is where the posterior distribution for the BBH model peaks [4], therefore leading to a stronger evidence. In fact, doing this we obtain $\log \mathcal{B}^{\rm PHOC},{}^{q=1}_{q=1} = -0.3$ and $\log \mathcal{B}^{\rm PHOC},{}^{q\neq 1}_{q=1} = 0.8$, revealing a slight preference for the PHOC model, despite the strong intrinsic bias for BBH models introduced by our standard distance prior, as discussed in the main text and in the Supplementary Table IV.

Waveform Model	$\log \mathcal{B}$	$\log \mathcal{L}_{Max}$
Quasi-circular Binary Black Hole	80.1	105.2
Quasi-circular Non-precessing Binary Black Hole	77.1	98.8
Quasi-circular Binary Black Hole ($q \leq 2$)	80.7	105.2
Quasi-circular Binary Black Hole ($q = 1$)	81.2	105.2
Head-on Equal-mass Proca Stars	80.9	106.7
Head-on Unequal-mass Proca Stars	82.0	106.5
Head-on Binary Black Hole	75.9	103.2

TABLE III. **Impact of Occam penalty on model selection:** We show the same results as in Table I, adding restricted BBH models that may obtain larger evidences than the full "vanilla" one (first row) due to the reduction of the Occam penalty. In particular, we explore the effect of restricting to aligned spins and also to mass ratios $q \leq 2$ and $q = 1$. None of these simplifications allows to make the models preferred wrt. our Proca star merger models.

6. *Evidence for Head-on BBHs*

For the HOC case, we did not explore the space spanned by the mass ratio and spins of the source in any systematic way. Instead, we performed simulations trying to maximise the Bayesian evidence (therefore populating the parameter space in a in-homogeneous way) until we determined it was not possible to keep increasing it. Fig. 6 shows the Bayesian evidence marginalised over extrinsic parameters and total mass for each of our HOC simulations, as a function of the mass ratio and the final spin. The largest evidences are yielded by sources with mass ratio $q \in [2,3]$, which can lead to larger final spins than equal-mass systems. We find that increasing the mass ratio and the final spin further does not lead to an increase of the evidence, nor the log likelihood. For this reason our simulations only reach a mass ratio $q = 4$.

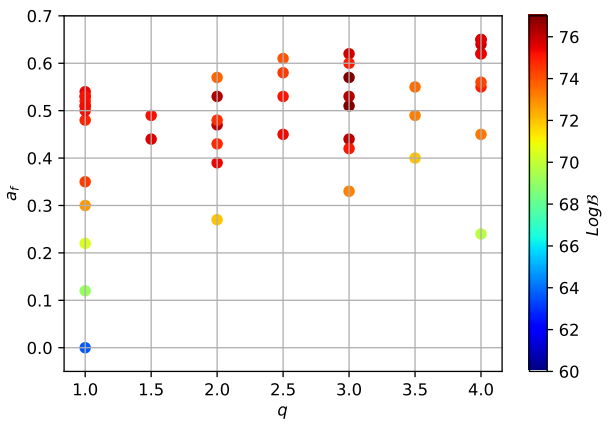

FIG. 6. **Numerical simulations for head-on BH mergers.** We label our simulations by the mass-ratio and the final-spin. The color code denotes the Bayesian evidence $\log \mathcal{B}$ obtained for each simulation, marginalised over the extrinsic parameters and the total mass of the source (Eq. 12).

Given our in-homogeneous family of HOCs, we cannot directly make use of to Eq. 8 to integrate Z as there is no parameter on which our simulations span an uniform grid. Instead, we interpolate the marginalised Bayesian evidence across an uniform grid in final spin and mass-ratio, and compute the evidence for the whole model as:

$$\mathcal{Z}_{\rm HOC} \approx \sum \mathcal{L}(d|(q,a_f), HOC)\, \pi(q,a_f)\, dq da_f, \qquad (11)$$

with

$$\mathcal{L}(d|q,a_f; HOC) = \int \mathcal{L}(d|(q,a_f),\hat{\theta}, HOC)\, \pi(\hat{\theta})\, d\hat{\theta}. \qquad (12)$$

Finally, given the evident lack of simulations below a final spin $a_f = 0.3$ we only include simulations with $a_f \geq 0.3$ in the above calculation.

7. *Constructing posterior distributions for HOC and PHOC*

Since the BBH model spans a continuous parameter space, we can trivially obtain posterior distributions on the different parameters marginalised over all other 14 parameters assuming given priors on these. However, our numerical simulations for HOCs and PHOCs span only a discrete set of mass ratios and spins. For this reason, for these models, and for each value of the mass ratio and spins, we obtain a discrete set of posterior parameter distributions for the extrinsic

Waveform Model	$\log \mathcal{B}(d_L)$	$\log \mathcal{L}_{Max}$
Quasi-circular Binary Black Hole	80.1	105.2
Head-on Equal-mass Proca Stars	83.5	106.7
Head-on Unequal-mass Proca Stars	84.3	106.5
Head-on Binary Black Hole	78.0	103.2

TABLE IV. **Bayesian evidence for our source models using a uniform-in-distance prior:** The first four rows show the natural Log Bayes Factor obtained for our different waveform models and corresponding maximum values of the Log Likelihood.

parameters and the total mass, collectively denoted by $\hat{\theta}$.

To construct distributions marginalised over the intrinsic parameters of the simulations, we draw from each individual distribution for fixed mass and spins, a number of random samples proportional to the corresponding Bayes Factor. Note that since our PHOC simulations are uniformly distributed in the parameter ω/μ_V, we are intrinsically assuming an uniform prior on this parameter. In particular, for the parameter ω/μ_V the distribution shown in Fig. 4 is given by $p(\omega/\mu_V) \propto \log \mathcal{B}(\omega/\mu_\mathcal{V})$.

Given that our HOC simulations do not distribute in a rather arbitrary and non-uniform way across the parameter space, we cannot quote posterior parameter distributions under the assumption of any reasonable prior. For this reason, the estimates provided for the total mass and distance for HOC cases in the main text should be taken as rather ballpark numbers.

SUPPLEMENTARY MATERIAL

Alternative distance prior

Standard parameter estimation assumes that gravitational-wave sources distribute uniformly in co-moving volume. While this is a sensible assumption, it does intrinsically favour loud sources like quasi-circular BH mergers, over weaker head-on BH mergers. In this section we investigate the impact of this prior on the results presented in the main text by repeating our analysis imposing a prior uniform in distance, and report the Log Bayes factors obtained for each of our models (see Table IV). As it is evident, a prior uniform in distance removes the intrinsic bias for loud sources, giving significantly larger evidences for the PHOC models than in the main text. Table V shows the corresponding parameter estimates, fully consistent with those obtained using the standard distance prior, albeit slighlty more noticeable (and expected) changes in the distance and redshift (to lower values), and the source-frame mass (to larger values). In particular, we obtain fully consistent results for the frequency and the particle mass characterising the bosonic field, as well as for the maximum PS mass.

Parameter	
Total / Final mass	$234^{+12}_{-16}\ M_\odot$
Final spin	$0.75^{+0.08}_{-0.04}\ M_\odot$
Inclination	$0.88^{+0.24}_{-0.35}$ rad
Azimuth	$0.60^{+0.66}_{-0.48}$ rad
Luminosity distance	520^{+274}_{-181} Mpc
Redshift	$0.10^{+0.03}_{-0.05}$
Total / Final redshifted mass	$259^{+8}_{-10}\ M_\odot$
Frequency of bosonic field	$0.892^{+0.016}_{-0.020}$
Boson mass	$8.65^{+0.77}_{-0.84}$ eV
Maximal boson star mass	$174^{+19}_{-12}\ M_\odot$

TABLE V. **Parameters of GW190521 assuming an equal-mass head-on merger of PSs and an uniform distance prior.** The result are consistent with those reported in Table II in the main text, despite expected differences in the luminosity distance, redshift and source-frame mass.

REFERENCES

[1] B. P. Abbott *et al.* (Virgo, LIGO Scientific), Phys. Rev. Lett. **116**, 061102 (2016), arXiv:1602.03837 [gr-qc].
[2] B. P. Abbott *et al.* (LIGO Scientific, Virgo), (2018), arXiv:1811.12907 [astro-ph.HE].
[3] M. Volonteri, The Astronomy and Astrophysics Review **18**, 279 (2010).
[4] Abbott *et al.* (LIGO Scientific, Virgo), Physical Review Letters **125** (2020), 10.1103/PhysRevLett.125.101102.
[5] J. Aasi *et al.*, Classical and Quantum Gravity **32**, 074001 (2015).
[6] F. Acernese *et al.* (Virgo Collaboration), Class. Quant. Grav. **32**, 024001 (2015), arXiv:1408.3978 [gr-qc].
[7] B. Abbott *et al.* (LIGO Scientific, Virgo), Astrophys. J. Lett. **900**, L13 (2020).
[8] I. M. Romero-Shaw, P. D. Lasky, E. Thrane, and J. Calderon Bustillo, "Gw190521: orbital eccentricity and signatures of dynamical formation in a binary black

hole merger signal," (2020), arXiv:2009.04771.
[9] V. Gayathri *et al.*, "Gw190521 as a highly eccentric black hole merger," (2020), In prep..
[10] A. Heger, C. L. Fryer, S. E. Woosley, N. Langer, and D. H. Hartmann, Astrophys. J. **591**, 288 (2003), arXiv:astro-ph/0212469 [astro-ph].
[11] J. Caldern Bustillo, N. Sanchis-Gual, A. Torres-Forn, and J. A. Font, "Confusing head-on and precessing intermediate-mass binary black hole mergers," (2020), arXiv:2009.01066.
[12] V. Cardoso and P. Pani, "Testing the nature of dark compact objects: a status report," (2019), arXiv:1904.05363.
[13] A. Arvanitaki, S. Dimopoulos, S. Dubovsky, N. Kaloper, and J. March-Russell, Physical Review D **81** (2010), 10.1103/physrevd.81.123530.
[14] S. L. Liebling and C. Palenzuela, Living reviews in relativity **20**, 5 (2017).
[15] M. Bezares, C. Palenzuela, and C. Bona, Physical Review D **95**, 124005 (2017).
[16] C. Palenzuela, P. Pani, M. Bezares, V. Cardoso, L. Lehner, and S. Liebling, Physical Review D **96**, 104058 (2017).
[17] N. Sanchis-Gual, C. Herdeiro, J. A. Font, E. Radu, and F. Di Giovanni, Physical Review D **99**, 024017 (2019).
[18] R. Brito, V. Cardoso, C. A. Herdeiro, and E. Radu, Physics Letters B **752**, 291 (2016).
[19] N. Sanchis-Gual, C. Herdeiro, E. Radu, J. C. Degollado, and J. A. Font, Physical Review D **95**, 104028 (2017).
[20] F. E. Schunck and E. W. Mielke, Class. Quant. Grav. **20**, R301 (2003), arXiv:0801.0307 [astro-ph].
[21] E. Seidel and W.-M. Suen, Physical Review Letters **72**, 2516 (1994).
[22] F. D. Giovanni, N. Sanchis-Gual, C. A. Herdeiro, and J. A. Font, Physical Review D **98** (2018), 10.1103/physrevd.98.064044.
[23] N. Sanchis-Gual, F. D. Giovanni, M. Zilhão, C. Herdeiro, P. Cerdá-Durán, J. Font, and E. Radu, Physical Review Letters **123** (2019), 10.1103/physrevlett.123.221101.
[24] Abbott *et al.*, "Gravitational wave open science center strain data release for gw190521, ligo open science center," (2020).
[25] V. Varma, S. E. Field, M. A. Scheel, J. Blackman, D. Gerosa, L. C. Stein, L. E. Kidder, and H. P. Pfeiffer, Physical Review Research **1** (2019), 10.1103/physrevresearch.1.033015.
[26] N. Sanchis-Gual, M. Zilhão, C. Herdeiro, F. Di Giovanni, J. A. Font, and E. Radu, arXiv preprint arXiv:2007.11584 (2020).
[27] R. M. Wald, in *Black Holes, Gravitational Radiation and the Universe: Essays in Honor of C.V. Vishveshwara* (1997) pp. 69–85, arXiv:gr-qc/9710068 [gr-qc].
[28] M. Maggiore, *Gravitational Waves: Volume 1: Theory and Experiments*, Gravitational Waves (OUP Oxford, 2008).
[29] P. Anninos, D. Hobill, E. Seidel, L. Smarr, and W.-M. Suen, Physical Review D **52**, 2044 (1995).
[30] C. Palenzuela, I. Olabarrieta, L. Lehner, and S. L. Liebling, Physical Review D **75**, 064005 (2007).
[31] P. B. Graff, A. Buonanno, and B. Sathyaprakash, Phys. Rev. **D92**, 022002 (2015), arXiv:1504.04766 [gr-qc].
[32] J. Calderón Bustillo, J. A. Clark, P. Laguna, and D. Shoemaker, Phys. Rev. Lett. **121**, 191102 (2018), arXiv:1806.11160 [gr-qc].
[33] J. Calderón Bustillo, C. Evans, J. A. Clark, G. Kim, P. Laguna, and D. Shoemaker, (2019), arXiv:1906.01153 [gr-qc].
[34] K. Chatziioannou *et al.*, (2019), arXiv:1903.06742 [gr-qc].
[35] (2020), arXiv:2004.08342 [astro-ph.HE].
[36] M. Baryakhtar, R. Lasenby, and M. Teo, Physical Review D **96**, 035019 (2017).
[37] V. Cardoso, Ó. J. Dias, G. S. Hartnett, M. Middleton, P. Pani, and J. E. Santos, Journal of Cosmology and Astroparticle Physics **2018**, 043 (2018).
[38] C. Palomba, S. DAntonio, P. Astone, S. Frasca, G. Intini, I. La Rosa, P. Leaci, S. Mastrogiovanni, A. L. Miller, F. Muciaccia, *et al.*, Physical review letters **123**, 171101 (2019).
[39] C. A. Herdeiro and E. Radu, Physical review letters **112**, 221101 (2014).
[40] C. Herdeiro, E. Radu, and H. Runarsson, Classical and Quantum Gravity **33**, 154001 (2016).
[41] W. E. East and F. Pretorius, Physical review letters **119**, 041101 (2017).
[42] B. Ganchev and J. E. Santos, Physical review letters **120**, 171101 (2018).
[43] J. C. Degollado, C. A. Herdeiro, and E. Radu, Physics Letters B **781**, 651 (2018).
[44] "Einstein toolkit: http://www.einsteintoolkit.org,".
[45] F. Loffler, J. Faber, E. Bentivegna, T. Bode, P. Diener, *et al.*, Class.Quant.Grav. **29**, 115001 (2012), arXiv:1111.3344 [gr-qc].
[46] M. Zilhão and F. Löffler, *Proceedings, Spring School on Numerical Relativity and High Energy Physics (NR/HEP2): Lisbon, Portugal, March 11-14, 2013*, Int. J. Mod. Phys. **A28**, 1340014 (2013), arXiv:1305.5299 [gr-qc].
[47] E. Schnetter, S. H. Hawley, and I. Hawke, Class. Quant. Grav. **21**, 1465 (2004), arXiv:gr-qc/0310042 [gr-qc].
[48] "Cactus: http://www.cactuscode.org.".
[49] M. Ansorg, B. Brügmann, and W. Tichy, Physical Review D **70**, 064011 (2004).
[50] H. Witek and M. Zilhão, "Canuda," `https://bitbucket.org/canuda/`.
[51] C. Reisswig and D. Pollney, Classical and Quantum Gravity **28**, 195015 (2011), arXiv:1006.1632 [gr-qc].
[52] G. Ashton *et al.*, Astrophys. J. Suppl. **241**, 27 (2019), arXiv:1811.02042 [astro-ph.IM].
[53] D. P. W. Veitch, John. and M. Pitkin, 10.5281/zenodo.592884.
[54] N. J. Cornish and T. B. Littenberg, Class. Quant. Grav. **32**, 135012 (2015), arXiv:1410.3835 [gr-qc].
[55] N. J. Cornish and T. B. Littenberg, Classical and Quantum Gravity **32**, 135012 (2015).
[56] L. S. Finn, Physical Review D **46**, 5236 (1992).
[57] J. D. Romano and N. J. Cornish, Living Reviews in Relativity **20** (2017), 10.1007/s41114-017-0004-1.
[58] C. Cutler and É. E. Flanagan, Physical Review D **49**, 2658 (1994).